Physical-informed deep learning prediction of solid and fluid mechanical properties of oxide glasses

Franck Pigeonneau, M. Rondet, O. de Lataulade, E. Hachem

Physical-informed deep learning prediction of solid and fluid mechanical properties of oxide glasses

F. Pigeonneau[a,*], M. Rondet[a], O. de Lataulade[b], E. Hachem[a]

[a] *MINES Paris, PSL University, CEMEF - Centre for material forming, CNRS UMR 7635, CS 10207, rue Claude Daunesse 06904 Sophia Antipolis Cedex, France*
[b] *L'Oréal Operations, Packaging Science Center, 9 rue Pierre Dreyfus 92110 Clichy, France*

Abstract

The deep learning technique is an efficient method to determine properties of unknown glass compositions. It is used to predict physical properties as density, Young's modulus, Poisson's ratio and three isokom temperatures of specific values of the dynamic viscosity. After a recall of models to determine the elasticity properties, the deep learning method is presented with the databases used to build data-sets. To predict density, the fitting is achieved on the molar volume with a large data-set. For the Young's modulus and according to the Makishima-Mackenzie's model, the fitting is done on the atomic packing fraction. The Poisson's ratio is determined according to the Makishima-Mackenzie's theory involving also the atomic packing fraction. For each prediction, a comparison with experimental data is provided. Finally, predictions are used to see which glass family is the more relevant to optimize the specific Young's modulus as a function of the "melting" temperature.

Keywords: glass, machine learning, density, Young's modulus, Poisson's ratio, dynamic viscosity

1. Introduction

Oxide glass is a unique material with transparency, high rigidity and chemical resistance, formability and unlimited recyclability. Therefore, glass is and will be a material in a wide range of applications in the future [1]. Mauro and Zanotto [2] listed major

*Corresponding author: Tel. +33 (4) 93 95 74 34.
Email address: franck.pigeonneau@minesparis.psl.eu (F. Pigeonneau)

challenges in the field of glass science and technology. Finding new glasses that can "*be produced on a large scale in a completely sustainable, environmentally friendly way*" or "*develop ultra-light, strong glass containers that reduce waste and energy consumption*" are examples drawn in [2]. Investigations in new glass compositions are then expected, purpose of our contribution.

According to Scholze [3], oxide glasses can have unlimited possible compositions. The sorting of oxides in glass network formers, modifiers and intermediates [3] gives a huge possibility of compositions. Since the pioneer contribution of Winkelmann and Schott [4], academic works have been devoted to composition-property relations. Using multi-linear regression methods and the additivity principle [5, chap. 6], the determination of the dynamic viscosity of glass forming liquids has been studied by Lakatos et al. [6], Fluegel [7] and Fluegel et al. [8] based on SciGlass database.

As pinpointed by Ravinder et al. [9], the research of new compositions is still based on "Edisonian" trial and error or physics-driven analysis. The recent emergence of Artificial Intelligence (AI) or more precisely Deep Learning opens new perspectives to speed up the finding of new glass compositions. The machine learning is useful for a large range of materials as for instance the predictions of chemical compounds for biological applications [10]. Jha et al. [11] detailed a model called ElemNet based on deep learning and applied to chemistry of materials.

In glass science, techniques based on machine learning have been presented by Mauro et al. [12] in which the combination of models at different scales is underlined. Tandia et al. [13] gave a general overview of the possibilities of machine learning to develop neural networks and genetic algorithms. For ternary silicate glasses, Bishnoi et al. [14] predicted the Young's modulus using Gaussian process regression to improve neural network results for sparse data-sets. Deng [15] developed deep learning methods to determine the mechanical properties of glasses in a reduced range of compositions. A comparison of techniques as random forest, K-Nearest neighbor, and neural networks has been also investigated in [15]. Ravinder et al. [16] described in more general case by applying deep learning to predict a large range of glass properties. Cassar [17] developed a physics-informed machine learning method to predict the viscosity of glass forming liquids. Zaki et al. [18] used machine learning methods to predict optical properties. The main con-

tributions of oxides on optical properties are identified by using the Shapley regression values provided in [19]. More recently, Le Losq and Baldoni [20] developed a machine learning modeling using also a physics-informed approach applied to alkali and alkaline-earth aluminosilicate glasses to predict mechanical properties. Apart from oxide glasses, investigations on metallic glasses have been recently done. Park et al. [21] identified constitutive equations of mechanical behavior of metallic glasses by coupling finite element analysis and artificial neural networks. Bobzin et al. [22] developed artificial neural networks to predict with a good efficacy glass transition, crystallization and liquidus temperatures. This partial overview shows the large possibility of the machine learning to predict properties or even glass compositions.

Despite of previous contributions, the development of deep learning models physically inspired on mechanical properties has to be investigated. It is well known in glass science that elastic properties are strongly related. In this contribution, the purpose is to establish the link between these properties and draw preliminary consequences in the choice of glass composition. First, theoretical models to determine the elastic properties will be recalled in section 2. The databases and the numerical method will be presented in section 3. Determination of mechanical properties will be then presented in section 4. The dynamic viscosity and its "melting", softening and annealing isokom temperatures are presented in section 5. Property charts are finally presented in section 6 before to summarize the work in section 7.

2. Solid mechanical properties of oxide glasses

Since the work of Makishima and Mackenzie [23, 24], theoretical models allow to determine the elastic properties of oxide glasses. Considering a glass composed by N oxides of general form $\mathrm{R}_{m_i}\mathrm{O}_{n_i}$ with a molar fraction x_i, the Young's modulus is given by

$$E = 2V_t\mathcal{G}, \tag{1}$$

with V_t the atomic packing fraction given by

$$V_t = \frac{\sum_{i=1}^{N} V_i x_i}{\frac{3}{\mathcal{V}_\mathcal{M}}}, \tag{2}$$

and $\mathcal{G}$

$$\mathcal{G} = \sum_{i=1}^{N} G_i x_i. \tag{3}$$

The factor V_i of i oxide is generally determined by the knowledge of Pauling's ionic radii of $R_{m_i}O_{n_i}$ oxide. The dissociation energy G_i of i oxide can be found in the original article of Makishima and Mackenzie [23] or more recently in the revisited model by Inaba et al. [25]. Finally $\mathcal{V}_\mathcal{M}$ is the molar volume defined by

$$\mathcal{V}_\mathcal{M} = \frac{\mathcal{M}}{\rho}, \tag{4}$$

with

$$\mathcal{M} = \sum_{i=1}^{N} \mathcal{M}_i x_i, \tag{5}$$

the molar mass of the glass.

The dissociation energy corresponds to an energy per unit volume equivalent to a pressure. Consequently, the atomic packing fraction is a dimensionless quantity of order of magnitude to one.

In [24, 26], the Poisson's ratio is given by

$$\nu = \frac{1}{2} - \frac{1}{6\alpha V_t}, \tag{6}$$

with α a numerical coefficient fitted on experimental data. In the original derivation of Makishima and Mackenzie [24], α is equal to 1.2 while Rocherullé et al. [26] proposed a value equal to 1.08.

Recently, Shi et al. [27] pinpointed that the Makishima and Mackenzie model underestimates the Young's modulus of a large amount of glass compositions. Shi et al. [27] attributed the disagreement to the atomic packing fraction which does not take into account the network connectivity [28]. Shi et al. [27] focused their investigations in the accurate determination of the atomic packing fraction by studying more than one hundred glasses.

In the following, a method based on deep learning method is proposed to determine the atomic packing fraction using large data-sets of glasses. It will then be possible to predict E and ν.

3. Databases and deep learning method

3.1. Databases

Data-sets used in the following are built with the commercial Interglad V8 database distributed by the New Glass Forum and an open version of SciGlass database available at https://github.com/epam/SciGlass. The former is searchable via a `Java` interface while the latter can be loaded with `GlassPy`, a `Python` module developed by Cassar [29]. The gathering of the two sources is achieved on a specific property. The oxide list is constituted from the classification provided in [3, 25] as follows

i) **network formers**: SiO_2, B_2O_3, P_2O_5, V_2O_5 and GeO_2;

ii) **network modifiers**: Na_2O, K_2O, Li_2O, CaO, MgO, SrO, BaO, Fe_2O_3, Y_2O_3, La_2O_3;

iii) **network intermediates**: Al_2O_3, TiO_2, ZrO_2, ZnO and PbO.

A cleaning is achieved by using the `Pandas` module of `Python` by the removal of duplicated sources. Glass for which the sum of molar fractions are not equal to 1 are dropped. Outliers on the property are removed by determination of the probability density function (PDF) of the property. To cancel these kind of outliers, the head and the tail of the PDF is cut using two filtering values, one for the low probability and one for the probability close to one. This method is efficient to remove the aberrant data. Outliers of each oxide are also removed by determining the PDF of molar fraction of each oxide. Data in the head and in the tail of the PDF are considered as not enough significant to be removed from the data-set.

3.2. Deep learning method

The fitting of a property is achieved using a deep learning method, i.e. with Artificial Neural Networks (ANN). Inputs or features are taken equal to the twenty molar fraction x_i of oxide i listed above with $i \in [1; p]$ and p=20. By definition, the vector $\boldsymbol{x}$ is the array of all molar fractions of the twenty oxides. Systematically, the property y is normalized as follows

$$\bar{y} = \frac{y - \langle y \rangle}{\sigma(y)}, \tag{7}$$

with $\langle y \rangle$ the expected value and $\sigma(y)$ the standard deviation of y. A Neural Network is defined by an input layer, here the p oxide molar fractions, K hidden layers composed by a number of "neurons", $N^{(k)}$ (with $k \in [1, K]$) and an output layer, here the property to compute. Each neural in the k hidden layer is defined by [30]:

$$h_i^{(k)}(\boldsymbol{x}) = g^{(k)} \left(\omega_{i0}^{(k)} + \sum_{j=1}^{N^{(k-1)}} \omega_{ij}^{(k)} h_j^{(k-1)} \right), \text{ for } i \in [1, N^{(k)}], \tag{8}$$

with $g^{(k)}$ the activation function of the k hidden layer and $\omega_{i0}^{(k)}$ and $\omega_{ij}^{(k)}$ parameters to compute. For the first layer, $h_j^{(k-1)}$ is simply equal to x_j.

Two or three hidden layers are taken with a neuron number equal to the number of oxides, i.e. $N^{(k)} = p$. According Le Losq and Baldoni [20], the Gaussian error linear units, "gelu", has been selected as activation functions in each hidden layer. A linear function is used for the output layer. This means that the predicted property is defined by [30]:

$$\bar{y}_j^{\text{ANN}}(\boldsymbol{x}) = \beta_0 + \sum_{j=1}^{N^{(K)}} \beta_j h_j^{(K)}, \tag{9}$$

with β_j for which j varies from 0 to $N^{(K)}$ parameters to fit.

The training consisting to compute all parameters $\omega_{ij}^{(k)}$ and β_j is achieved with an Adam solver with a learning rate around 2×10^{-4}. The splitting of the data-set in training, validation and test is done with ratios of $[0.6; 0.2; 0.2]$ respectively. The Mean Squared Error (MSE), defined by [30]

$$MSE(\bar{y}) = \frac{1}{M} \sum_{j=1}^{M} \left(\bar{y}_j - \bar{y}_j^{\text{ANN}} \right)^2, \tag{10}$$

is chosen as a loss function with M the sample number of data-set. To avoid as much as possible over-fitting, the numbers of hidden layers and neurons are chosen the smallest as possible. The assessment of the model accuracy is measured using the R^2 statistic quantity defined as follows [30]

$$R^2(\bar{y}) = 1 - \frac{\sum_{j=1}^{M} \left(\bar{y}_j - \bar{y}_j^{\text{ANN}} \right)^2}{\sum_{j=1}^{M} \bar{y}_j^2}. \tag{11}$$

The closest to one $R^2(\bar{y})$ is, the best the ANN model is.

The numerical method has been developed with the module `keras` of `Python`. `Python` scripts to prepare data-sets, training and predicted properties are available on the GitHub repository at the following address:
https://github.com/franck-pigeonneau/deeplearningforglass.

4. Mechanical property predictions

4.1. Molar volume

Mass density is one of the properties for which data are the most abundant because it is easy to measure with high accuracy and of course important to know for customers. From a combination of the Interglad V8 and SciGlass databases, a data-set of 64 420 glasses with the 20 oxides has been constituted. Figure 1a gives the bar plot of number of glasses for each oxide of the data-set. Silica is particularly very well represented since this oxide is involved in more than 40 000 glass compositions. The least abundant oxides are Y_2O_3 and V_2O_5. These two oxides are present in 1577 and 2217 samples respectively. To control how large is the molar fraction for each oxide, Figure 1b depicts the bar plot of the maximum of molar fraction, $\max(x_i)$, for the 20 oxides found in the data-set. This information will be useful to avoid extrapolations of the ANN model outside of the composition of the data-set. The network formers are a full range of molar fraction. The alkali and alkaline earth oxides are large ranges of molar fractions. The smallest of the maximum of molar fraction is obtained for ZrO_2 which is equal to 0.3.

To see the range of density in the data-set, Figure 1c depicts the probability density function as a function of ρ given in $\mathrm{kg/m^3}$. The smallest density is equal to $1.78 \times 10^3\,\mathrm{kg/m^3}$ while the largest is around $7 \times 10^3\,\mathrm{kg/m^3}$. The most probable density is around to $2.5 \times 10^3\,\mathrm{kg/m^3}$. The long tail has been conserved because glasses with a large amount of lead oxide have a large density.

The density prediction as a function of composition has been studied in detail by Huggins [31] and Huggins and Sun [32] for silicate glasses. Instead of to fit the density, Huggins [31] suggests to fit the inverse of the density. In the original work of Huggins, the inverse of the density is given as a function of the mass fraction. If each oxide is

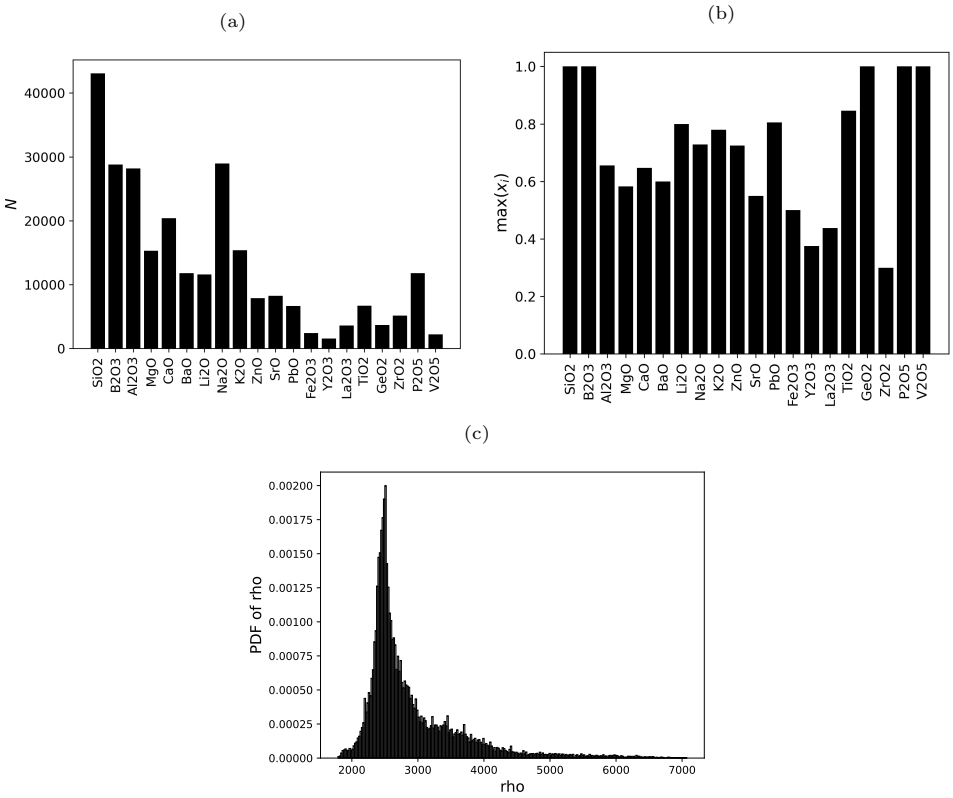

Figure 1: Summary of the data-set on the density at room temperature gathered 64 420 glasses: (a) number of glasses containing the oxides listed in abscissa (b) maximum of the molar fraction, $\max(x_i)$, for each oxide and (c) probability density function of ρ in kg/m^3.

written as $\mathrm{M}_{n_i}\mathrm{O}_{m_i}$, the inverse of ρ is given by

$$\frac{1}{\rho} = \sum_{i=1}^{N} \left[(k + b_{\mathrm{SiO_2}})\, n_i + m_i c_i \right] \frac{y_i}{\mathcal{M}_i}, \tag{12}$$

with k a constant depending of the cooling rate, $b_{\mathrm{SiO_2}}$ and c_i parameters fitted as a function of the composition [32], y_i the mass fraction and $\mathcal{M}_i$ the molar mass of the oxide i. The two factors n_i and m_i correspond to the numbers of cation and oxygen in the oxide i. Using the relation linked the molar and mass fraction, the molar volume is then given by

$$\mathcal{V}_{\mathcal{M}} = \sum_{i=1}^{N} \left[(k + b_{\mathrm{SiO_2}})\, n_i + m_i c_i \right] x_i. \tag{13}$$

The above equation suggests to fit the molar volume as a function of the oxide molar

fractions. Huggins [31] developed a method to find parameters k, b_{SiO_2} and c_i in a small range of composition. Extend for a large range of composition the method of Huggins is a cumbersome task. An artificial neural network is then used to fit directly the molar volume as a function of the molar fraction of a large range of oxides. The density of the data-set is taken here to determine the molar volume using equation (4).

The neural network to predict $\mathcal{V}_{\mathcal{M}}$ is composed by three hidden layers composed by twenty neurons. The activation function are "gelu" for the hidden layers and linear for the output layer. After the training of the data over two thousand of epochs, the loss function is provided in Figure 2a. MSE decreases very quickly over the first fifty epochs. After 500 iterations, the loss function reaches a plateau. To improve the MSE, the training stage is repeated few times by shuffling the data-set at the beginning of the fitting. By this way, the MSE reaches a value of 2×10^{-3}.

The prediction-data-set comparison for the training, validation and test sub-sets are provided in Figure 2b-d for molar volume in cm^3/mol. Dashed lines give the prediction with $\pm 20\,\%$ of error while solid line is the prediction without error. Each R^2-score, defined by eq. (11), is reported in each sub-figure. R^2-scores for the three sub-sets are very close to one meaning that the variability in the prediction is well captured with the ANN model. Only one data is outside of the bandwidth of $20\,\%$ of error. The density of results is large which is an essential point to have a large range of exploration for the determination of the molar volume.

Although the prediction-data curves allow to assess the ANN model, the predictions are compared to experimental data to quantify the accuracy of the model and to control over-fitting. It is expected that the data used to the comparison exercise can be in the data-set but it is useful to see as far the predicted values are from the experimental values.

Figure 3a depicts the density for three binary glasses of SiO_2-R_2O as a function of the alkaline molar fraction x_{R_2O}. Alkali considered are Na, K and Li. Experimental data represented with symbols in Figure 3a are extracted from the handbook of Bansal and Doremus [33]. The predictions of the ANN model are plotted in solid lines while experimental data are depicted with discrete symbols. The increase of the density due to the introduction of Na and K is very well reproduced with the ANN model. The value

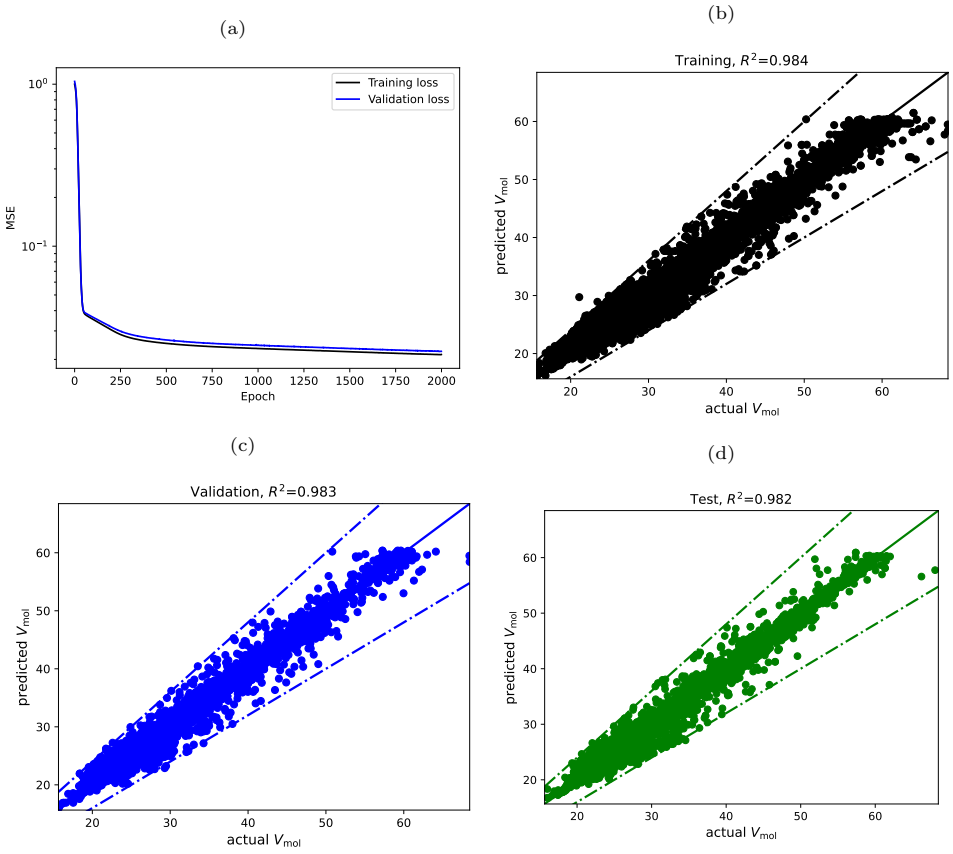

Figure 2: (a) Loss function (Mean Squared Error) as a function of epoch by fitting $\mathcal{V}_{\mathcal{M}}$ with an ANN model with three hidden layers of 20 neurons and predicted molar volume in (cm^3/mol) as a function of database values for the (b) training, (c) validation and (d) test sub-sets.

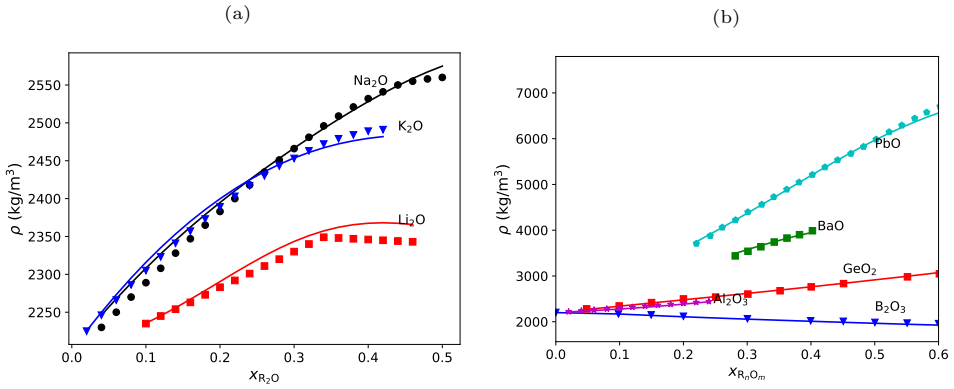

Figure 3: Density (kg/m^3) of binary glasses as a function of molar fraction for (a) SiO_2-R_2O system with R=Na, K and Li and (b) SiO_2-R_nO_m system with R=B, Ba, Ge, Al and Pb. Symbols are experimental data according to Bansal and Doremus [33]. Solid lines are the prediction values from the ANN model on $\mathcal{V}_{\mathcal{M}}$.

of the molar fraction for which the density of SiO_2-K_2O glass is less that the density of SiO_2-Na_2O system is very well found with the ANN model. The least effect of the lithium on the increase of density is also well captured by the ANN model. The ANN model overestimates the density when x_{Li_2O} is larger than 0.33. The non-linear monotonic increase of ρ as a function of x_{R_2O} is well reproduced from the ANN model.

Density for SiO_2-R_nO_m system with R equal to B, Ba, Ge, Al and Pb is depicted in Figure 3b. Each oxide has a particular contribution on the glass density. Globally, the introduction of these elements leads to a linear behavior of ρ as a function of molar fraction of R_nO_m. The range of density with the serial of oxides is large since ρ can change from 1.8×10^3 to 6.6×10^3 kg/m^3. While the introduction of boron oxide leads to a decrease of density, the lead oxide increases strongly the density. The ANN model predicts with a good agreement the behavior of each oxide in the full range of molar fraction.

The comparison exercise is extended to ternary alkaline-silica glasses of composition SiO_2-Na_2O-Li_2O. Once again experimental data are taken from the handbook of Bansal and Doremus [33]. They reported the effect on the substitution of Na_2O by Li_2O when the total alkaline molar content stays equal to 25 %. Figure 4 depicts the glass density as a function of $x_{Li_2O}/(x_{Li_2O}+x_{Na_2O})$. As already seen before in Figure 3a, the introduction

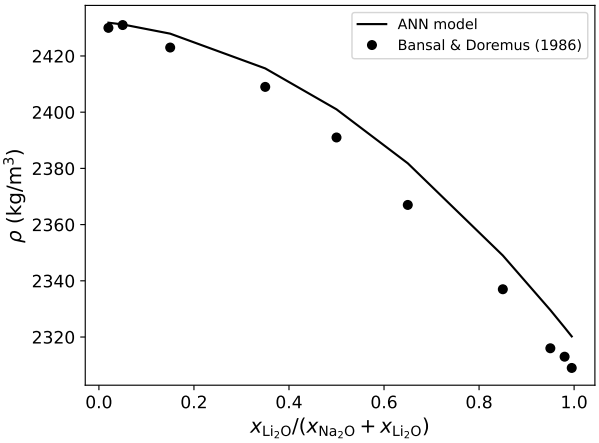

Figure 4: Density (kg/m^3) of ternary glasses SiO_2-Na_2O-Li_2O as a function of $x_{Li_2O}/(x_{Li_2O} + x_{Na_2O})$.

of the lithium oxide leads to a decrease of ρ. The ANN model reproduces very well the decrease of the density when Na_2O is substituted by Li_2O.

The high level of accuracy and the large range of molar fractions is an important behavior of the present model since it will be used in the following.

4.2. Young's modulus

The Young's modulus, E, is an essential property in a large range of applications. It is expected to have a large values of E to enhance for instance the fracture toughness [34, 35]. Data-set coming from the two databases SciGlass and Interglad V8 has been built as previously on the glass density. The list of oxides is similar to the previous section with twenty oxides listed in subsection 3.1. The data-set on E gathered from the two databases is composed by 10 864 glasses. Bar plot of the glass number for each oxide is given in Figure 5a. The number of samples are abundant for the two network formers, SiO_2 and B_2O_3. Conversely, a poor presence of V_2O_5 and GeO_2 is noticeable. In the data-set, only 399 and 103 glasses contain V_2O_5 and GeO_2 respectively. Figure 5b summarizes the bar plot of the maximum of molar fraction for the 20 oxides. Globally, network formers and modifiers are large ranges of composition while it is more reduced for the network intermediates. The maxima of molar fraction are only 0.1 for F_2O_3 and ZrO_2. Figure 5c provides the probability density function of E determined from the data-set. The total range of variation of the Young's modulus is between 17 and 110 GPa.

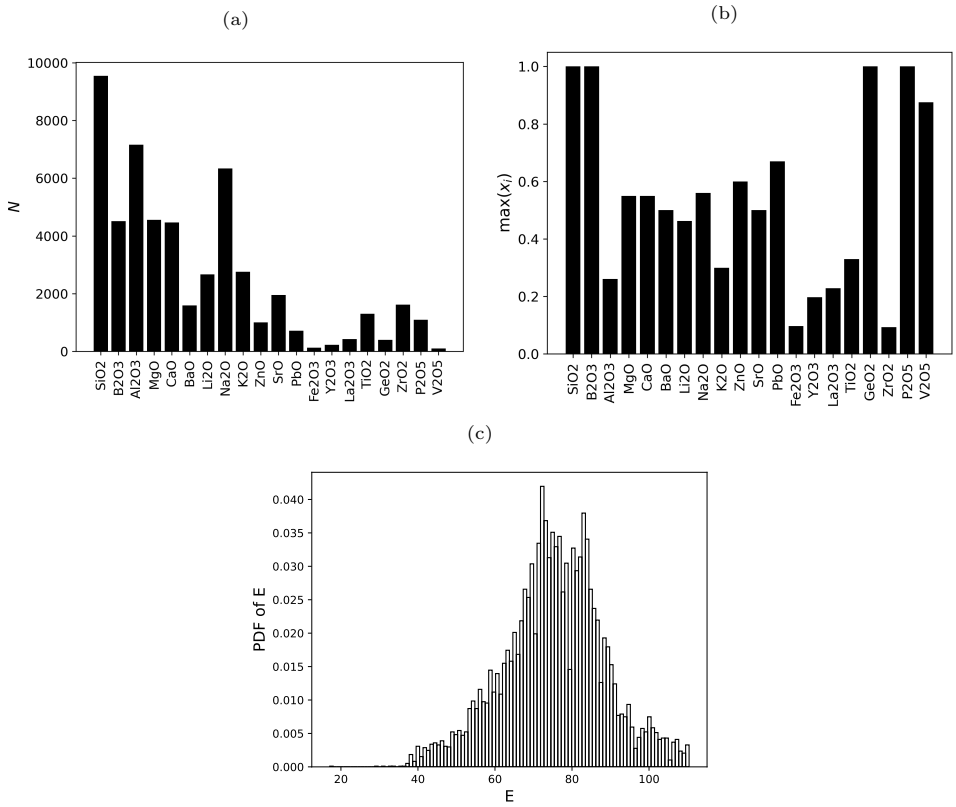

Figure 5: Summary of the data-set on the Young's modulus gathered 10 864 glasses: (a) number of glasses containing the oxides listed in abscissa (b) maximum of the molar fraction, $\max(x_i)$, for each oxide and (c) Probability density function of E in GPa.

The smallest values of E have been preserved to study the specific behavior of glasses rich in B_2O_3. Even if it is expected that E could be reached value larger than 160 GPa for glasses composed of BeO, Al_2O_3 or ZrO_2 [5], glasses of our data-set never reach this high magnitude due to a poor occurrence of glasses with these oxides, see Figure 5b.

As pinpointed in section 2, Makishima and Mackenzie [23] proposed a general model to determine the Young's modulus linked to the dissociation energy of each oxide and to the atomic packing fraction. The model has been recently revisited by Shi et al. [27] in which a particular attention is drawn on the atomic packing fraction. Here, the deep learning technique is used to determine the atomic packing fraction given by the following

relation:

$$V_t^{\text{ANN}}(\boldsymbol{x}) = \frac{E}{2\mathcal{G}}, \tag{14}$$

with $\boldsymbol{x}$ the oxide vector. The values of V_t is determined from the data-set of the Young's modulus. The energy $\mathcal{G}$ is computed from dissociation energies given by Inaba et al. [25]. According to Soga [34], Inaba et al. [25] and more recently Bishnoi et al. [14], network formers and intermediates can have various coordination states. It is well established for B_2O_3 and P_2O_5 that the Makishima-Mackenzie's model needs improvements to predict E [25]. Since the dissociation energy depends directly on the oxygen coordination number, it is expected that the Young's modulus depends on the coordination state. In this work, only one dissociation energy of B_2O_3 has been taken equal to this one of B_2O_3 in oxygen coordination four, i.e. $G_{B_2O_3}$=82.8 GPa. For P_2O_5, the modified dissociation energy is taken from the value of Inaba et al. [25].

An ANN model with two hidden layers with 20 neurons for each layer has been developed to fit V_t. Training with three and four hidden layers have been achieved which do not significantly improve the RSM. Moreover, comparisons with the experimental data are worse than the ANN predictions with only two hidden layers. The activation function is "gelu" for hidden layers and a linear function for the output layer. The training sub-set is composed by 60 % while the validation sub-set by 20 % of the total data-set. As previously, the loss function is the mean squared error shown in Figure 6a over 2000 epochs. The minimum of the MSE on the normalized unknown is less than 3×10^{-1} for the training sub-set. To improve the convergence of the model, the training stage has been run few times by shuffling the data-set at the beginning of the training. After these training iterations, Figure 6b gives prediction versus data-set values of V_t for the training sub-set. R^2-score indicated in Figure 6b is acceptable. A large amount of data gives an atomic packing fraction in range of $[0.3; 1]$. The largest value obtained from the data-set is equal to 1.3 while the smallest value is equal to 0.1. The comparison of the prediction versus data-set values for the validation and test sub-sets are given in Figure 6c and Figure 6d. The R^2-score indicates that the prediction reproduced with a high level of confidence the data-set values. As previously, dashed lines correspond to curves obtained with an error of ± 20 %.

To control the accuracy of the ANN model on V_t, a comparison exercise on E is

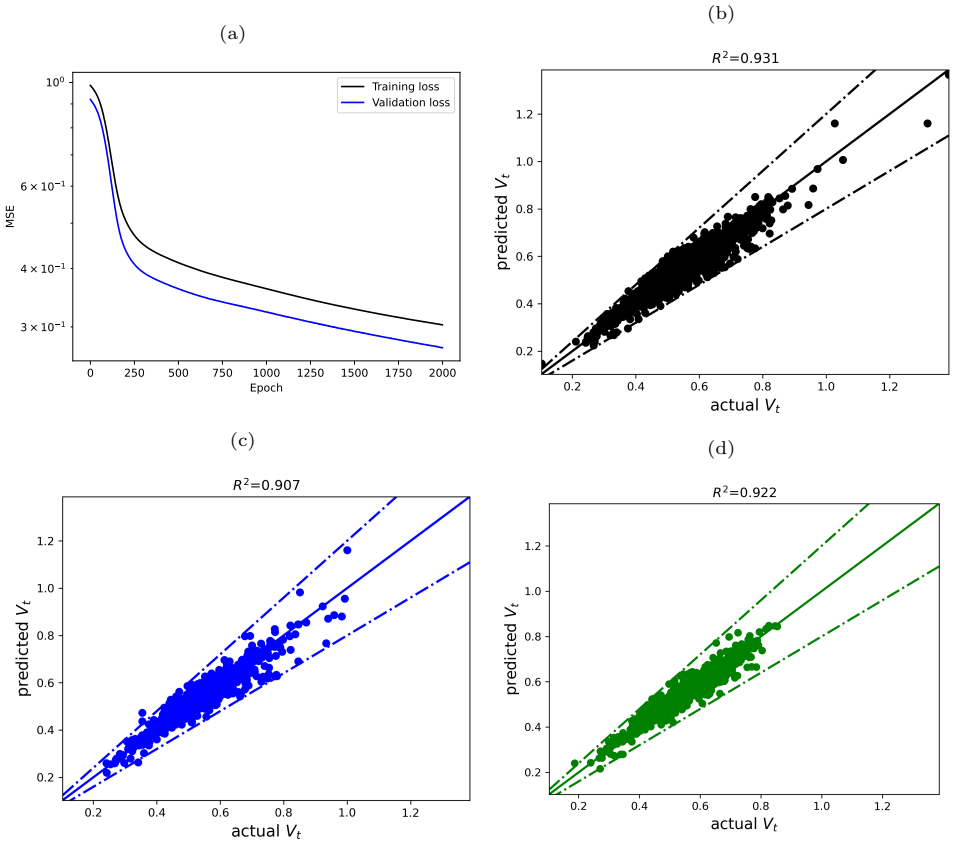

Figure 6: (a) Loss function (Mean Squared Error) as a function of epoch by fitting V_t with an ANN model of two hidden layers of 20 neurons and predicted V_t as a function of data-set values for (b) training, (c) validation and (d) test sub-sets.

done as previously on the molar volume. The Young's modulus is computed with the ANN model previously fitted for binary systems SiO_2-R_2O for R equal to Na, K and Li. Results are compared to the experimental data of Manghnani [36]. Figure 7 depicts E versus the molar fraction of alkaline oxide. The solid lines correspond to the results obtained with the model based on the determination of the atomic packing fraction. Symbols are the data taken from Manghnani [36]. As observed experimental, predictions of Young's modulus from the ANN model reproduced the decrease of E for Na and K. Conversely, glasses with lithium oxide exhibits an increase of E very well found with the ANN model. These large values of E with Li_2O can be explained partially by the fact

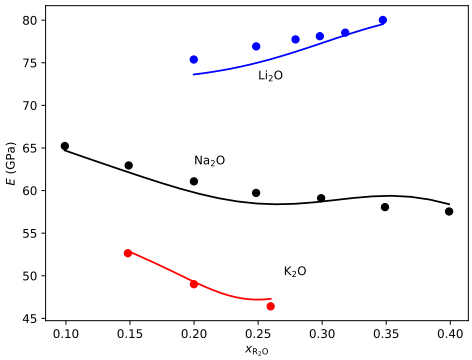

Figure 7: E as a function of x_{R_2O} in the system SiO_2-R_2O. Solid lines are results from the ANN model determining (14), and symbols are experimental data from Manghnani [36].

of the dissociation energy of Li_2O is larger than for Na_2O and K_2O, see table provided in [25].

The Young's modulus has been also predicted in the ternary system $SiO_2-Na_2O-B_2O_3$ with three values of Na_2O molar fraction and a variation of $x_{B_2O_3}$. Experimental values of E are taken from Imaoka et al. [37]. Figure 8 depicts E as a function of $x_{B_2O_3}$ for three values of molar fraction of Na_2O. The Young's modulus are determined using the ANN model with Eq. (14) and represented in solid lines. Symbols in Figure 8 are the values coming from Inaba et al. [25]. Globally, the introduction of boron oxide leads to a decrease of E. For x_{Na_2O}=0.1, Inaba et al. [25] give a value of E equal to 17.1 GPa when $x_{B_2O_3}$=0.85. The ANN model gives a value close to 40 GPa. The non-monotonic behavior of E observed experimentally is well reproduced with the ANN model. When the molar fraction of sodium oxide is equal to 20 %, boron oxide has the least effect since the Young's modulus is approximately equal to 50 GPa for the largest boron content. The non-monotonic behavior of E with $x_{B_2O_3}$ is well predicted by the ANN model which gives a maximum of E for $x_{B_2O_3}$=0.2. For the largest molar fraction of Na_2O, predictions are less satisfying. Nevertheless, experimental data provided by Imaoka et al. [37] for x_{Na_2O}=0.25 are scattered.

Even if the effect of the oxygen coordination has not explicitly taken into account in the ANN model, the prediction on borate glasses is quite satisfying. The assessment of the ANN model is also evaluated on the borate and phosphate glasses studied by Inaba

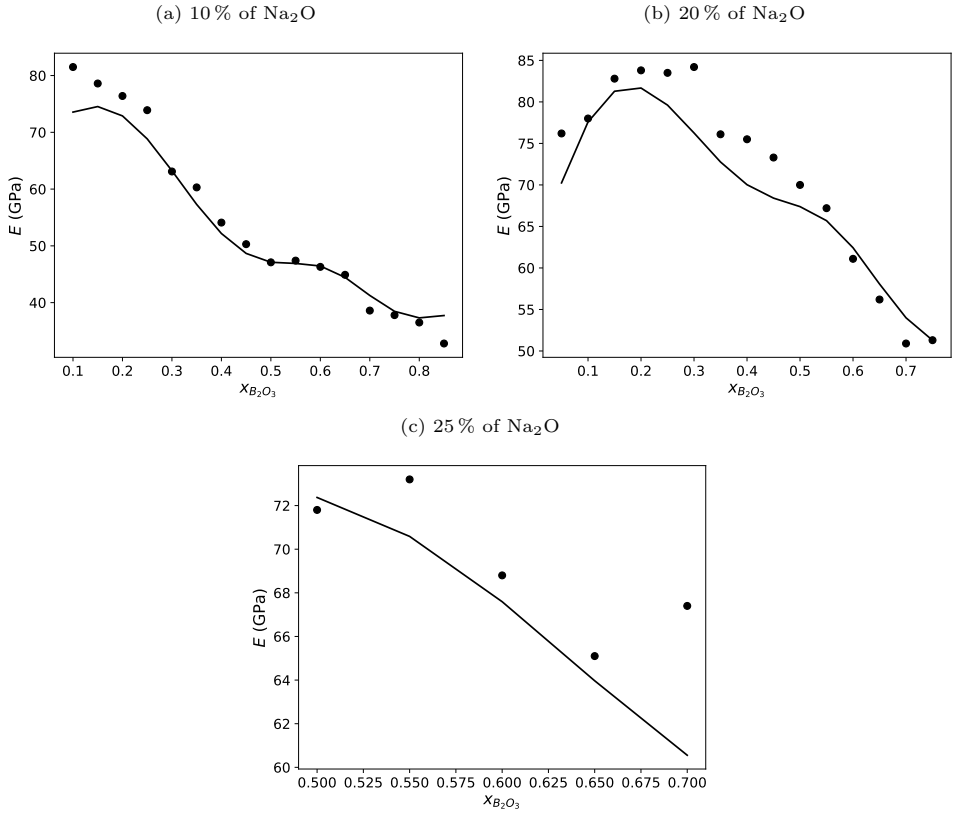

Figure 8: E as a function of $x_{B_2O_3}$ in the ternary system $SiO_2-Na_2O-B_2O_3$ for (a) x_{Na_2O}=10 %, (b) x_{Na_2O}=20 % and (c) x_{Na_2O}=25 %. Solid lines are the predictions of the ANN model on (14), dashed lines are the predictions of the ANN model on E. Symbols come from data of Imaoka et al. [37].

et al. [25]. The Young's moduli for the 21 glasses provided in [25] have been determined with the ANN model. Figure 9 depicts the predicted versus measured E for borate glasses in blue symbols. The range of magnitude of E is important for these borate glasses. The Young's modulus varies between 17 and 90 GPa. Even if the oxygen coordination number is not explicitly accounted for, the agreement is satisfying. It is significantly good for E larger than 50 GPa, i.e. for glasses with less amount of B_2O_3. The overall error is equal to 12 %.

According to Inaba et al. [25], the prediction of Young's modulus of phosphate glasses from the Makishima-Mackensie's model needs improvement due to the specific structure of phosphate glasses. Inaba et al. [25] modified the dissociation energy of P_2O_5 used

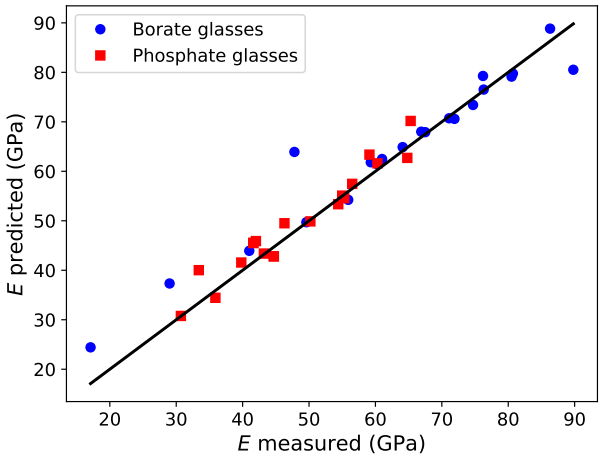

Figure 9: E predicted by the ANN model as a function of E measured experimentally from [25] for borate glasses (blue symbol) and phosphate glasses (red symbol).

in our model. Figure 9 presents the predicted versus measured of E for 20 phosphate glasses in red symbols. The agreement between predicted and measured of E is good. The overall error is equal to 6 %.

This comparison exercise shows that the ANN model developed on the atomic packing fraction can learn with a high level of fidelity the general aspect of the structural configuration of glasses.

4.3. Poisson's ratio

As recalled in section 2, the Poisson's ratio can be determined from the knowledge of the atomic packing fraction, V_t. From the previous sub-section, the determination of V_t is computed as a function of the glass composition. To evaluate equation (6), a data-set of the Poisson's ratio has been constituted. It gathers 1464 glasses composed with the same list of oxides used in previous sub-sections. Even with the two databases, the amount of data giving the Poisson's ratio is smaller than for the two previous properties.

Bar plots of occurrence and the range of molar fractions are reported in Figure 10a and Figure 10b. PbO, Y_2O_3 and V_2O_5 oxides are poorly represented. Figure 10c shows the probability density function of the Poisson's ratio which is spread over a range of $[0.17; 0.32]$ with an average value around 0.23.

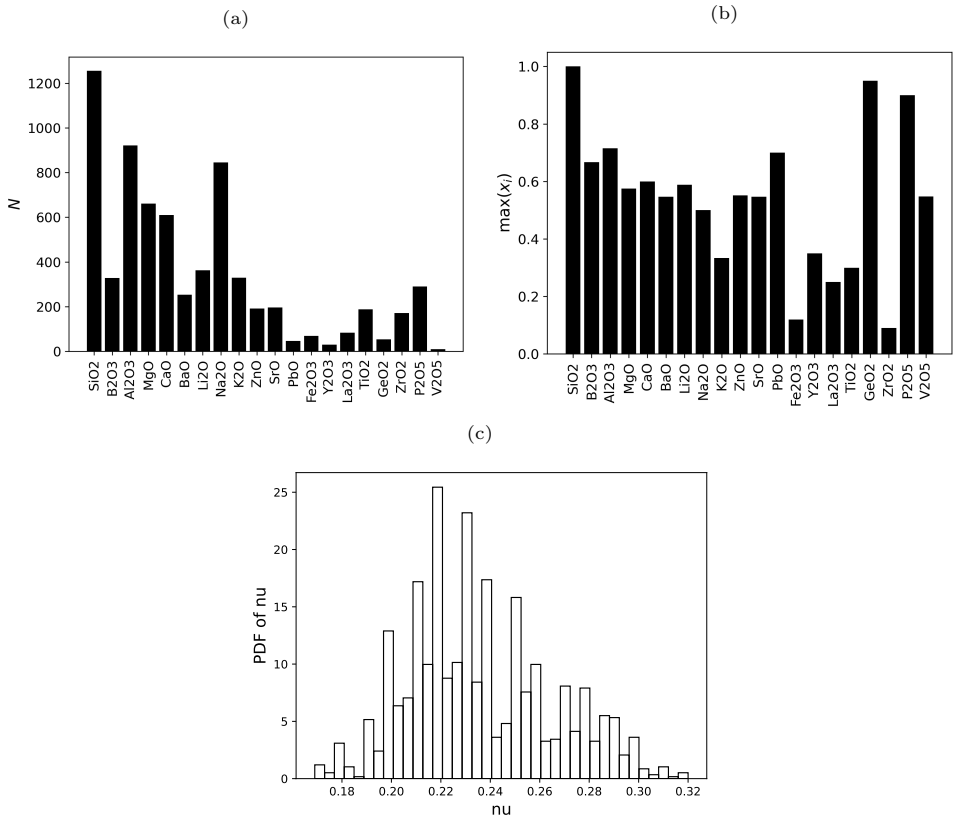

Figure 10: Summary of the data-set on the Poisson's ratio gathered 1464 glasses: (a) number of glasses containing the oxides listed in abscissa (b) maximum of the molar fraction, max(x_i), for each oxide and (c) probability density function of ν.

The data-set has been used to control the validity of equation (6) with the values of α proposed by Makishima and Mackenzie [24] and Rocherullé et al. [26]. Figure 11a depicts the predicted Poisson's ratio with α=1.2 as a function of the Poisson's ratio coming from the data-set. Roughly, predictions with α=1.2 are shifted to larger values of ν. This means that equation (6) with α=1.2 over-estimates the experimental Poisson's ratio. R^2-score is negative meaning that the prediction is not satisfying. Figure 11a shows that the data are very scattered. When α=1.08 as proposed in [26], the prediction of ν is globally better than these ones obtained with α=1.2 as it is shown in Figure 11b. Roughly, the predictions do not overestimate the Poisson's ratio. Nevertheless, the scattering stays important since R^2-score is only equal to 0.3.

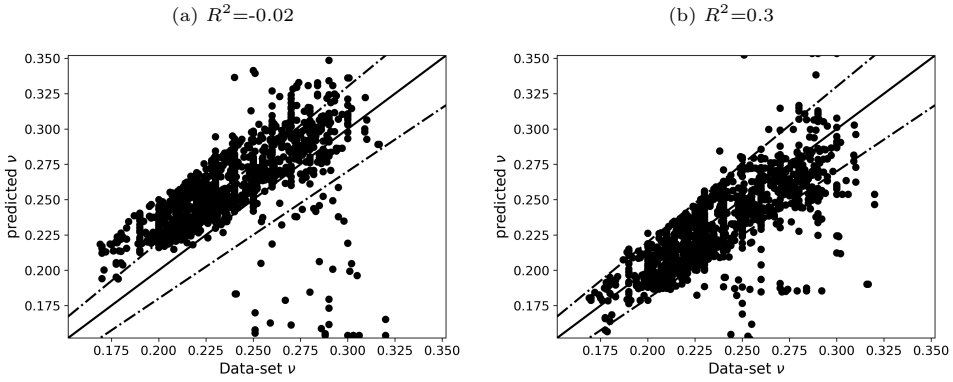

Figure 11: Prediction of ν from equation (6) as a function of data-set values of ν for (a) α=1.2 and (b) α=1.08.

To improve the prediction of (6), an ANN model has been developed to compute α with three hidden layers and 20 neurons for each layer. Activation functions are the same of previous models. From the data-set of ν, the atomic packing fraction is computed from the ANN model developed in previous section. The training needs few (around 10) runs to obtain a loss function sufficiently small. The prediction versus data-set values on the normalized α is summarized in Figure 12. The dashed lines represent predictions with $\pm 10\,\%$. The average value of α is equal to 1.11 and the standard deviation is 0.12. As expected $\bar{\alpha}$ is distributed around the zero value. Nevertheless, the distribution is large meaning that the value of α changes significantly. This explains why it is difficult to predict the Poisson's ratio for a large range of coefficient with only one value of α. In Figure 12, prediction versus data-set values is plotted for the three sub-sets of data. R^2-score on the training sub-set is very close to one while is around 0.93 for the validation sub-set and 0.9 on the test sub-set.

The model to predict α has been used to determine the Poisson's ratio using equation (6). Using the data-set on ν, the comparison is provided in Figure 13. The prediction values are close to the data-set values since R^2-score is equal to 0.98. Dashed lines correspond to a prediction with $\pm 10\,\%$ of error. Globally, apart from few data, the prediction is below to $10\,\%$ of disagreement. The standard deviation of the normalized error $(\nu^{\text{ANN}} - \nu)/\nu$ is equal to $2\,\%$.

Predictions of ν are compared to experimental values found in [5] for ternary glasses

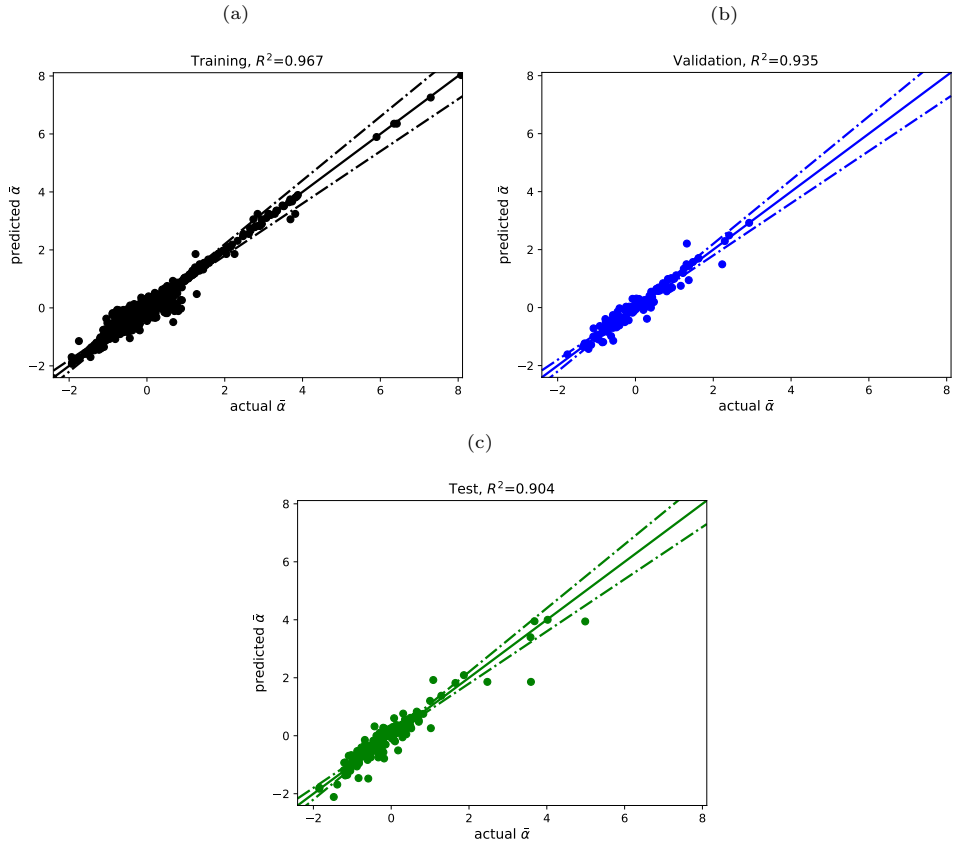

Figure 12: Predicted $\bar{\alpha}$ as a function of data-set values for (a) training, (b) validation and (c) test subsets.

of [5SiO_2-Na_2O-xRO]. Five elements have been tested. In Figure 14a, ν is plotted as a function of x corresponding to the mole of RO with R=Ba, Sr and Mg. Solid lines correspond to the predicted values while symbols correspond to experimental data according to Varshneya and Mauro [5]. The introduction of these three elements in the glass composition leads to an increase of the Poisson's ratio. The largest enhancement is observed in Figure 14a for Ba and the smallest for Mg. This observation is also verified with the prediction of ν even if the disagreement is more important for small values of x. The increase of the Poisson's ratio is also observed in Figure 14b in which R is equal to Zn and Ca. Once again, the prediction underestimates ν. The best prediction is observed for Ca for which experimental and predicted values are close when $x \geq$1.5.

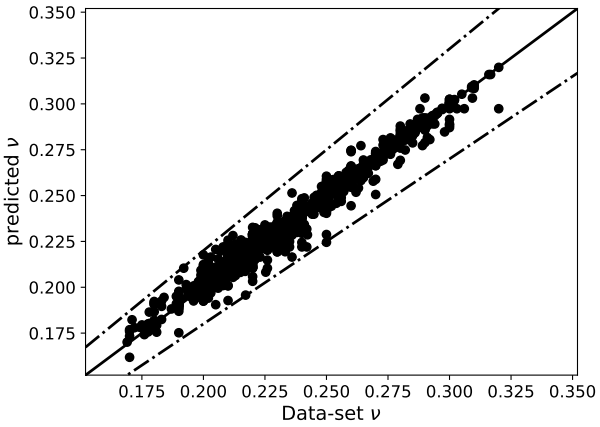

Figure 13: Predicted versus data-set values of ν. The prediction has been computed from equation (6) with α determined with the ANN model. R^2-score is equal to 0.98.

(a) R=Ba, Sr and Mg

(b) R=Zn and Ca

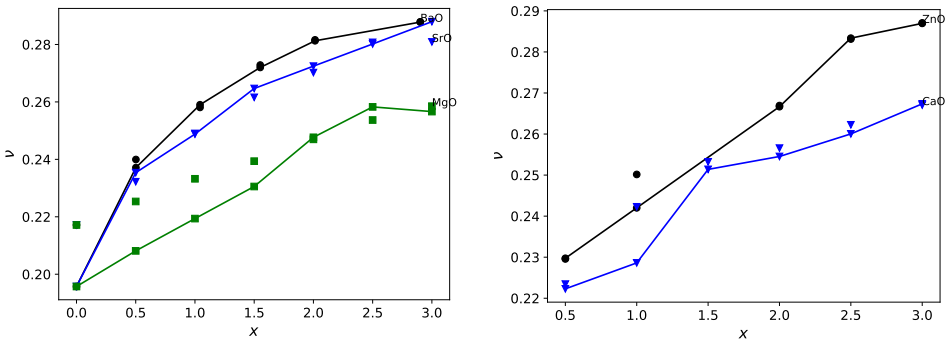

Figure 14: ν as a function of x in the [$5SiO_2$-Na_2O-xRO] system with x the mole of RO with (a) R=Ba, Sr and Mg and (b) R=Zn and Ca. Solid lines are the prediction results obtained with equation (6) and α determined with the ANN model. Symbols are plotted from data taken in [5].

The fitting of an ANN model on α using also an ANN model on V_t improves significantly the prediction of the Poisson's ratio. Nevertheless, the predictions are perfectible. To be more accurate, a larger data-set should be needed to improve the model training.

5. Dynamic viscosity

Beside the previous mechanical properties, other quantities have to be determined relevant for the glass melting. Among other things, the dynamic viscosity is needed to determine the rate of bubble rising in a glass-forming liquid. As well, this property is required in the computational fluid dynamics to determine the flow field [38]. More generally, all steps in the glass making are defined as a function of specific values of the dynamic viscosity [7]. In geophysics, the dynamic viscosity of silicate liquids is also important to define the nature of the eruption of a volcano [39].

As well known in glass sciences, the dynamic viscosity depends on temperature. Conversely to the majority of liquids, the dynamic viscosity of a glass forming liquid has a non-Arrherian temperature behavior [40]. From the different laws proposed in the literature and presented in the textbook of Varshneya and Mauro [5], the Vogel-Fulcher-Tammann's (VFT) law is the most commonly used for applications with enough accuracy [3] and in particular for the temperature larger than the glass transition temperature T_g. The glass viscosity is then determined from the following relation:

$$\log(\eta) = A + \frac{B}{T - T_0}, \tag{15}$$

with A, B and T_0 three coefficients depending on glass composition. To find these three factors with η in Pa $\cdot$ s, three isokom temperatures are used:

i) "melting" temperature T_m for which $\log(\eta)$ =1;

ii) softening (Littleton point) temperature T_s for which $\log(\eta)$ =6.65;

iii) annealing temperature T_g for which $\log(\eta)$ =12.

Here, the melting temperature is taken for a dynamic viscosity less than the values of Fluegel [7] who chose a $\log(\eta)$ =1.5. As pinpointed by Angell [41], the annealing temperature is close to the glass transition temperature since all viscosities plotted as

a function of T_g/T converge towards a unique point for which the viscosity is equal to $10^{12}\,\mathrm{Pa}\cdot\mathrm{s}$ when $T = T_g$.

5.1. Isokom temperatures T_m, T_s and T_g

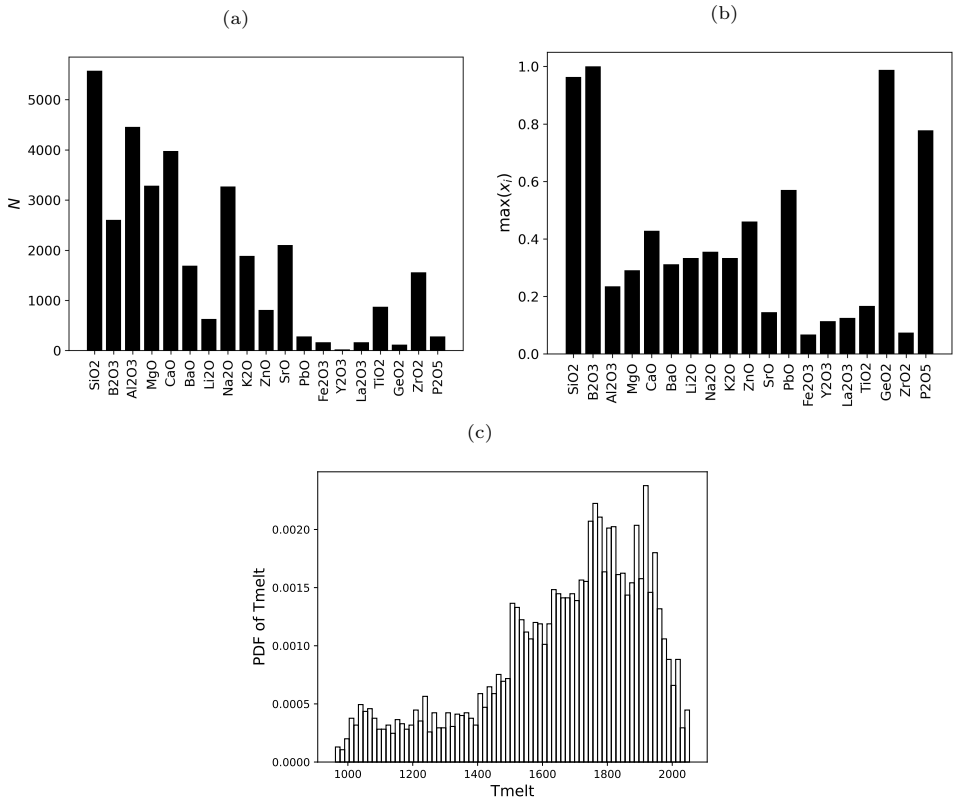

Figure 15: Summary of the data-set on T_m gathered 5995 glasses: (a) number of glasses containing the oxides listed in abscissa (b) maximum of the molar fraction, $\max(x_i)$, for each oxide and (c) probability density function of T_m in K.

Three data-sets have been constituted using the two databases already presented above. The data-set for the melting temperature is composed by 5995 glasses. Only 19 oxides have been considered due to the lack of data for V_2O_5. Figure 15a summarizes the bar plot of oxides in the data-set. Apart from P_2O_5 and GeO_2, the other network formers are well represented. It is the same for the network modifiers while for the intermediates are least present in glass compositions. Figure 15b provides the bar plot of maximum

of molar fraction for each oxide. The molar fraction are low for Fe_2O_3 and ZrO_2. The probability density function of T_m in K is provided in Figure 15c showing that T_m varies over a range of 1000 K. The largest values of probability density function are observed for T_m larger than 1500 K.

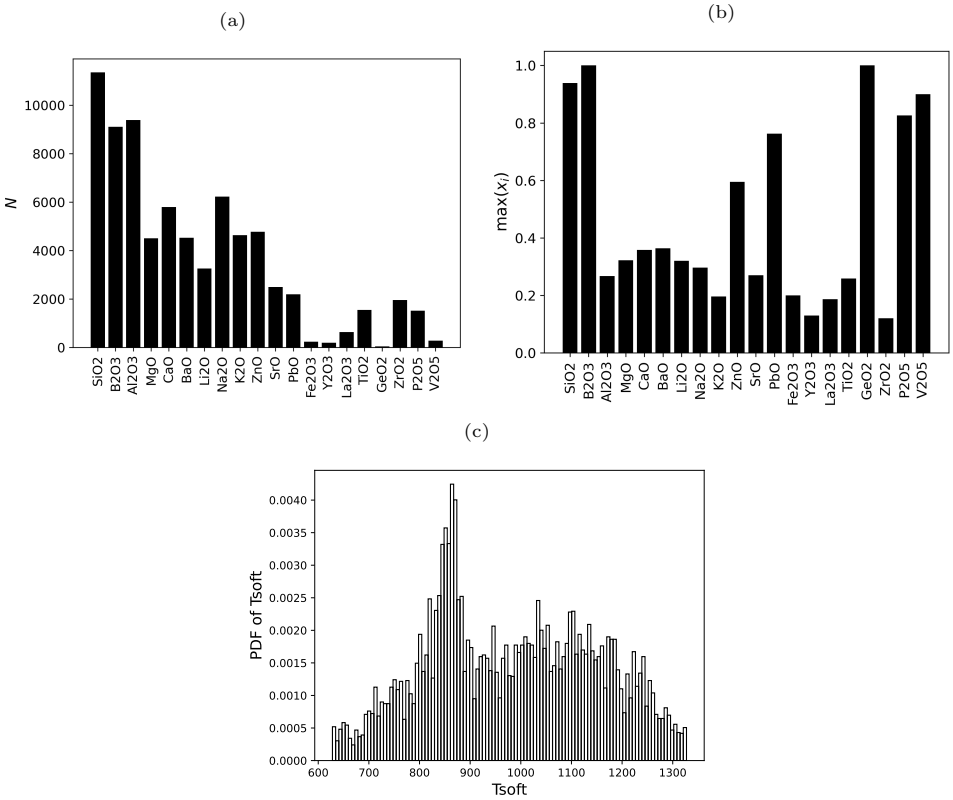

Figure 16: Summary of the data-set on T_s gathered 12531 glasses: (a) number of glasses containing the oxides listed in abscissa (b) maximum of the molar fraction, max(x_i), for each oxide and (c) probability density function of T_s in K.

For softening temperature, the data-set is composed by 12 531 glasses with the twenty oxides listed in subsection 3.1. The bar plot depicted in Figure 16a shows that the first twelve oxides are very well represented. The data-set lacks of the network former GeO_2. Glasses with V_2O_5, Fe_2O_3 and Y_2O_3 are also scarce in the data-set. As shown in Figure 16b, the ranges of molar fractions of network formers are significant for this data-set. The smallest molar fractions are obtained for Y_2O_3 and ZrO_2. The probability

density function of T_s in K is depicted in Figure 16c. Softening temperature ranges over 630 to 1330 K. The most probable T_s is around 870 K in the data-set.

Finally, the data-set for the annealing temperature is constituted by 6613 glasses with a bar plot given in Figure 17a showing a poor representation of V_2O_3 and Y_2O_3 only fifteen glasses are composed by these oxides. Apart from F_2O_3 and ZrO_2, Figure 17b shows that the maximum of molar fractions for the rest of oxides is larger than 0.1. The probability density function is represented in Figure 17c in which T_g varies over 550 to 1190 K.

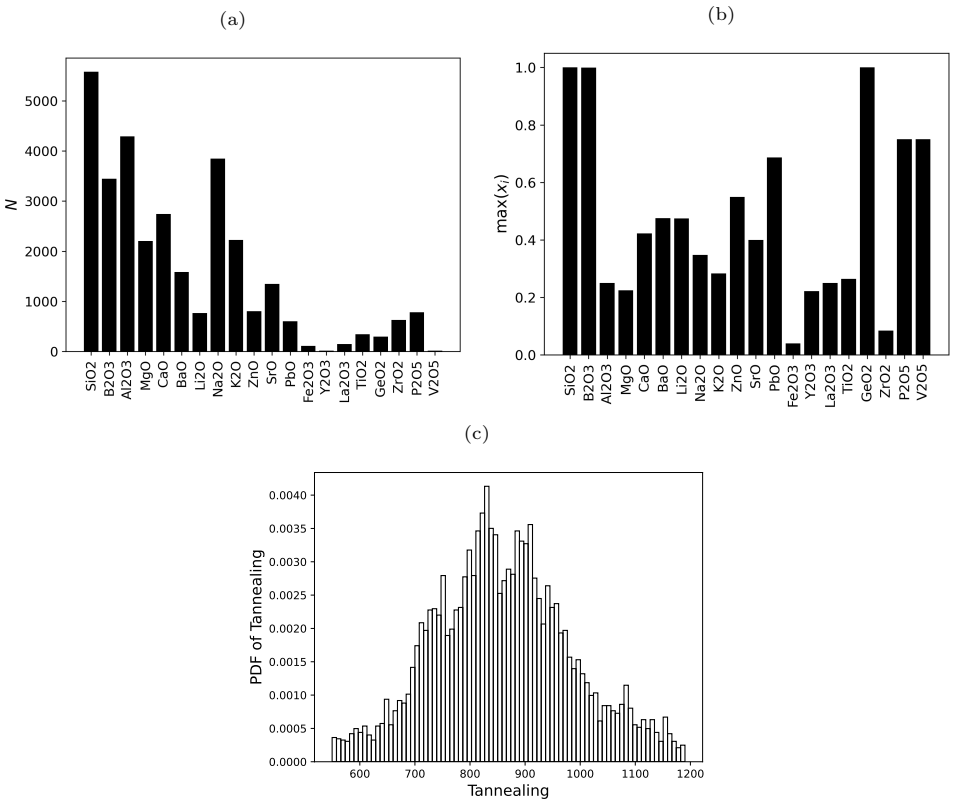

Figure 17: Summary of the data-set on T_g gathered 6613 glasses: (a) number of glasses containing the oxides listed in abscissa (b) maximum of the molar fraction, $\max(x_i)$, for each oxide and (c) probability density function of T_g in K.

For the three isokom temperatures, T_m, T_s and T_g, artificial neural networks of three hidden layers are used. As previously, the activation function of hidden layers is "gelu"

while for the output layer a linear function is chosen. The behavior of the loss function obtained during the fitting of the model on T_m is shown in Figure 18a. The convergence is fast over the first 200 epochs. The mean square error decreases slower for the larger epochs. Predictions versus data-set values for the training, validation and test sub-sets are provided in Figure 18b, Figure 18c and Figure 18d. Dashed-lines correspond to a prediction with an error of 10 %. R^2-scores are also reported in each figure. Globally, the model predicts very well the melting temperature since R^2 coefficient is close to one.

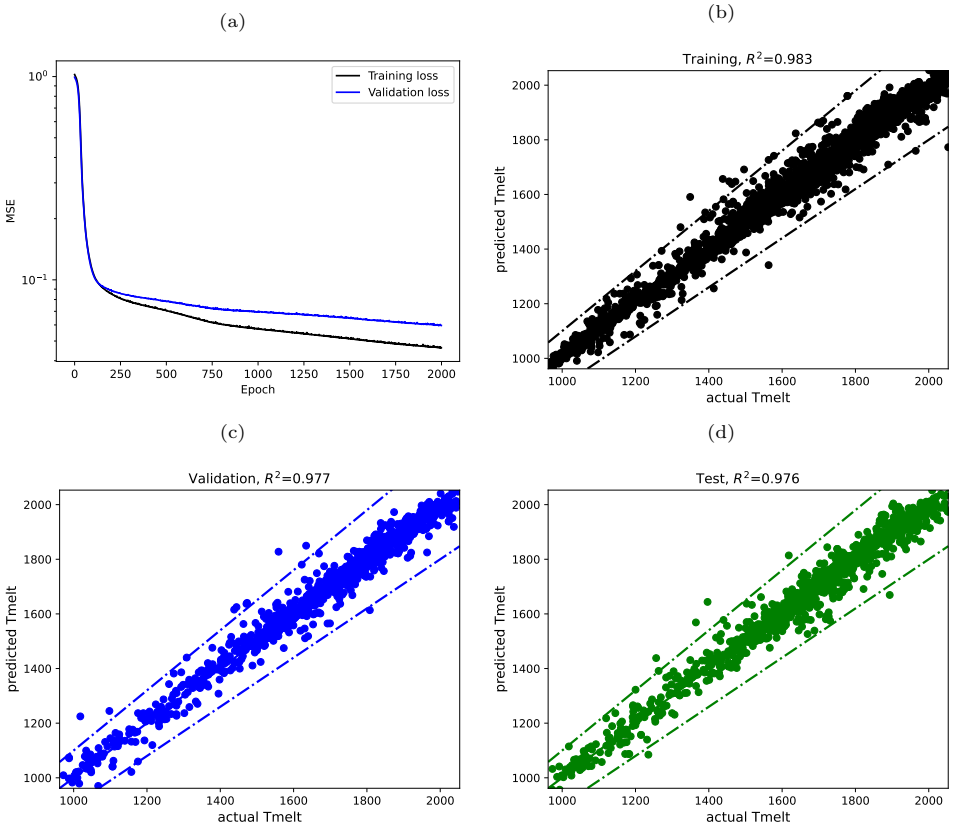

Figure 18: (a) Loss function (Mean Squared Error) as a function of epoch by fitting T_m with an ANN model with three hidden layers of 20 neurons and predicted T_m in (K) as a function of database values for (b) training, (c) validation and (d) test sub-sets.

The mean squared error behavior obtained for the fitting of T_s is given in Figure 19a. The rate of convergence is high at the beginning of the fitting process. It becomes low after 250 iterations. The comparison of prediction and data-set values for the training

sub-set is shown in Figure 19b. Due to the large number of glasses for the data-set of T_s, the density of data is large. The data scattering stays low since data-set values are predicted in the range of $\pm 10\,\%$ of error. R^2-score on the training sub-set is equal to 0.98. Equivalent behaviors are observed for the validation and test sub-sets depicted in Figure 19c and Figure 19d. The data scatterings are little more important. However, R^2-scores are also very close to one for both sub-sets.

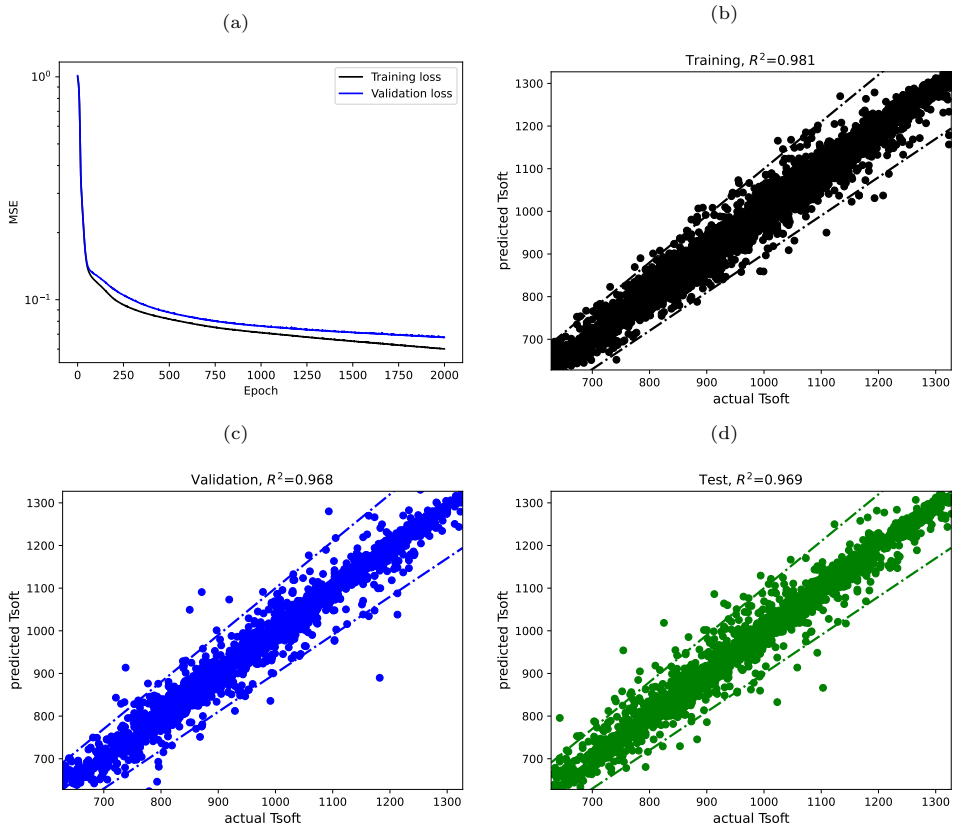

Figure 19: (a) Loss function (Mean Squared Error) as a function of epoch by fitting T_s with an ANN model with three hidden layers of 20 neurons and predicted T_s in (K) as a function of database values for (b) training, (c) validation and (d) test sub-sets.

The convergence behavior for the fitting of T_g is given in Figure 20a in which the rate of convergence is once again very high over the first 200 epochs. After, the rate of convergence stays uniform meaning that the convergence is exponential but with a low rate of convergence. To increase the accuracy of prediction, the training stage has been

repeated few times until to have the curves of prediction shown in Figure 20b, Figure 20c and Figure 20d for the training, validation and test sub-sets. The dashed lines are the bounds of prediction with $\pm 10\,\%$. R^2-score obtained on the training sub-set is equal to 0.99 while it is equal to 0.834 and 0.975 for the validation and test sub-sets respectively. For the three sub-sets, the density of values close to the diagonal line is large. Few predictions for the validation and test sub-sets are outside of the $20\,\%$ bandwidth.

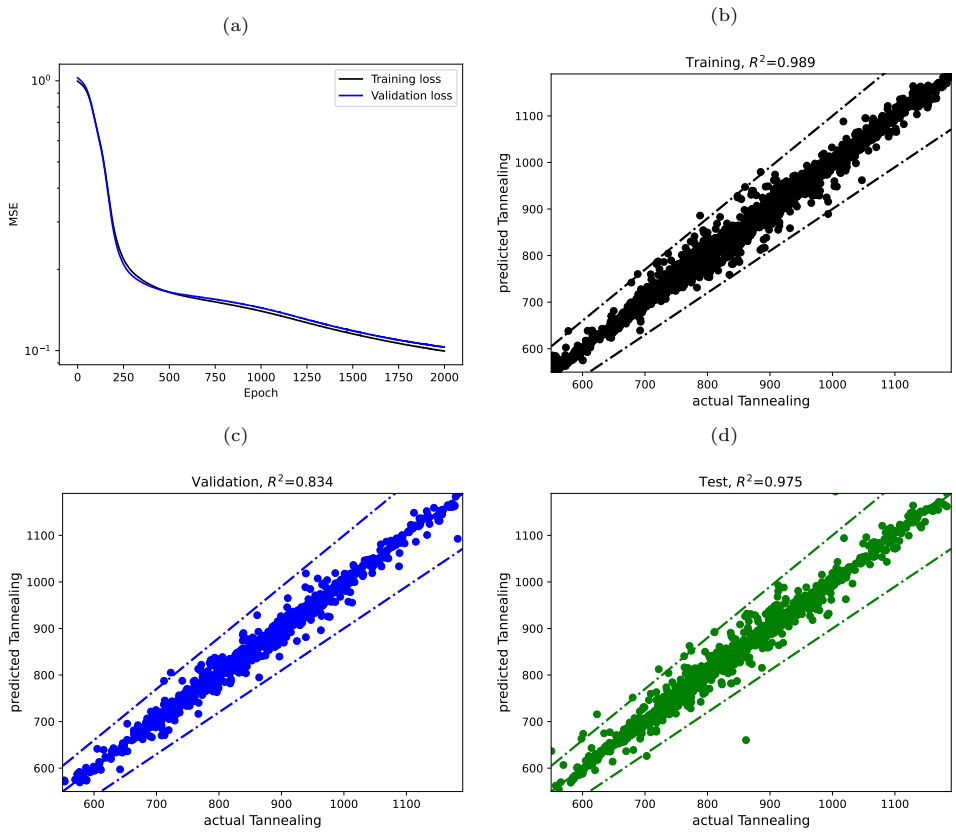

Figure 20: (a) Loss function (Mean Squared Error) as a function of epoch by fitting T_g with an ANN model with three hidden layers of 20 neurons and predicted T_g in (K) as a function of database values for (b) training, (c) validation and (d) test sub-sets.

5.2. Predictions of η versus T

From the knowledge of these three isokom temperatures, the three parameters of the VFT's law, eq. (15), can be determined. Numerical predictions have been compared

with dynamic viscosities of four typical glasses given in [42]. The glass compositions of container, float, TV and E glasses are given in Table 1. Roughly, the first two glasses are silico-soda-lime glasses. Float glass contains a larger amount of MgO. The particularity of the E glass is the larger amounts of Al_2O_3 and B_2O_3.

Table 1: Compositions in (mol %) of four glasses according to Seward [42] corresponding to container, float, TV and E glasses.

SiO_2	Al_2O_3	B_2O_3	MgO	CaO	SrO	BaO	Na_2O	K_2O	TiO_2	ZrO_2	ZnO	Fe_2O_3
74.38	1.28	0.00	0.20	10.51	0.01	0.10	13.30	0.29	0.008	0.00	0.00	0.036
72.93	0.13	0.00	3.84	8.740	0.00	0.00	13.74	0.03	0.017	0.00	0.00	0.109
61.53	2.06	0.00	0.00	0.050	9.19	9.23	7.640	7.55	0.430	1.39	0.51	0.037
56.60	14.8	7.04	4.33	18.20	0.00	0.00	0.630	0.00	0.580	0.00	0.00	0.350

Figure 21 depicts the behavior of η as a function of T in SI units. Solid lines are the predictions of η using equation (15) with the three coefficients determined with ANN models on T_m, T_s and T_g. Symbols come from data gathered in [42]. Viscosities for the container and float glasses are reproduced with ANN models. The role playing by the change in composition are also well reproduced in the two other glasses.

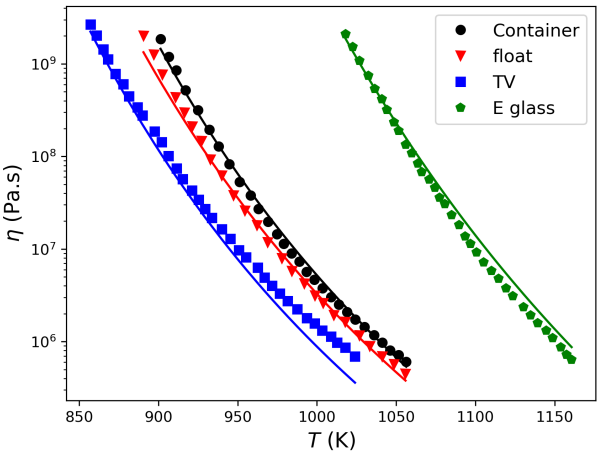

Figure 21: η in Pa $\cdot$ s as a function of T in K for container, float, TV and E glasses with compositions given in Table 1. Solid lines are the predicted viscosities with ANN models and symbols are data given in [42].

6. Property charts

To describe materials, Ashby [43] proposes to plot properties under various charts. A same approach has been also proposed by Ravinder et al. [16] and Zaki et al. [18]. To do the same, four glass families have been considered summarized in Table 2. The first family is a soda-lime-silica glass with the same molar fraction of Na_2O and CaO. For the second family, the silice oxide is subtituted to B_2O_3 by an amount of 0.1. For the alumino-silicate family, the average molar fraction of Al_2O_3 is reduced to 0.2 to be in the range of data-sets. For the phospho-silicate glass family, the molar fraction of P_2O_5 is set equal to 0.4 reducing the amount of SiO_2 to 0.3. The molar fractions of Na_2O and CaO do not change in the four families. The composition of the phospho-silicate glass family has been inspired to the recent patent [44] on glasses with low melting temperature. To determine the charts, the compositions are changed randomly around the average compositions given in Table 2. The glass compositions are completed with other oxides in the random order and with a random molar fraction in such a way that the sum of the molar fraction is equal to 1. To avoid to extrapolate outside of glass compositions used in the various training detailed above, the molar fraction of each oxide is bounded by the minimum of the maximum of molar fraction of oxide i in the data-sets. For each family, 10 000 of compositions are used.

Table 2: Glass compositions of the four families given in molar fraction.

Oxide	SiO_2	B_2O_3	Al_2O_3	P_2O_5	Na_2O	CaO
Soda-lime-silica	0.7	0	0	0	0.1	0.1
Boro-silicate	0.6	0.1	0	0	0.1	0.1
Alumino-silicate	0.6	0	0.1	0	0.1	0.1
Phospho-silicate	0.3	0	0	0.4	0.1	0.1

Mechanically, large Young's modulus is favorable. In the same time, to have a lighter material, it is better to minimize the density. Consequently, the ratio E/ρ corresponding to a specific modulus [43] has to be optimized. As it is well known in elasticity, the sound velocities in solid are proportional to $\sqrt{E/\rho}$ [45, Chap. 2]. Here, $\sqrt{E/\rho}$ is plotted as a function of T_m in Figure 22. Melting temperature is important to know from the

point of view of glass melting. It is the characteristic temperature to remove efficiency bubbles from the glass forming liquid. A reduction of T_m from 1500 to 1200 °C leads to a decrease of the energetic power of 20 %.

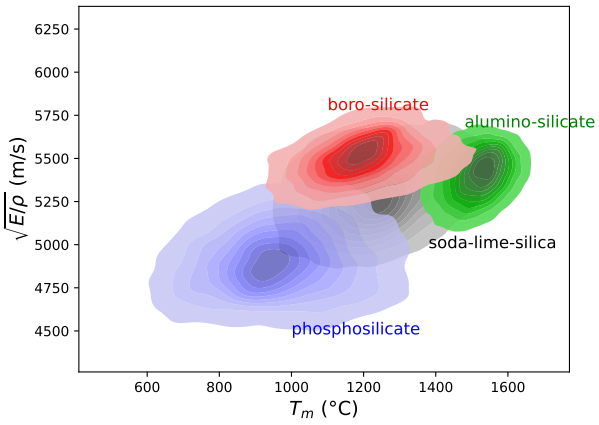

Figure 22: $\sqrt{E/\rho}$ in $(\mathrm{m\,s^{-1}})$ as a function of T_m in (°C) for the four glass families. Soda-lime-silica family is depicted in black, boro-silicate family in red, alumino-silicate family in green and phospho-silicate family in blue.

The predictions for the four families are drawn in Figure 22. The soda-lime-silica glass family is given in black while boro-silicate one in red. The alumino-silicate family is plotted in green and the phospho-silicate family in blue. Globally, soda-lime-silica and alumino-silicate families are in the same range of $[\sqrt{E/\rho}, T_m]$. Nevertheless, alumino-silicate family has the largest T_m. The boro-silicate family gives the optimal $\sqrt{E/\rho}$ with intermediate melting temperatures. The largest range of variation is observed for the phospho-silicate family for which the melting temperature can change from 600 to 1300 °C. This family as underlined in [44] offers a large interest to provide glasses with high mechanical properties with low melting temperature.

To complete the previous chart, Figure 23 gives the chart in $[T_m, T_g]$ diagram. Roughly, the four families are localized on the same trend. The smallest T_m and T_g are obtaining for the phospho-silica family. The largest T_m and T_g are obtained for the alumino-silicate family. The boro-silicate and soda-lime-silica families give the quasi same range of T_m. The range of T_g is large for the soda-lime-silica family. The phospho-silicate family explores large ranges of T_m and T_g.

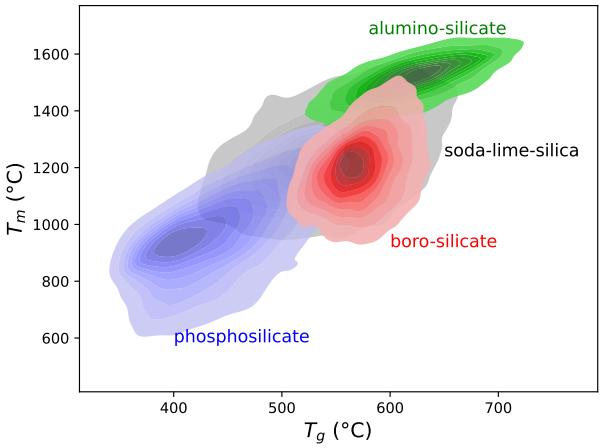

Figure 23: T_m in (°C) as a function of T_g in (°C) for the four glass families. Soda-lime-silica family is depicted in black, boro-silicate family in red, alumino-silicate family in green and phospho-silicate family in blue.

Even if the boro-silicate family presents interested features, boron oxide is volatile which is an important issue from the industrial point of view. Conversely, phospho-silicate family gives an alternative possibility of glass composition.

7. Synthesis and perspectives

Mechanical properties have been determined using deep learning method. First, two databases have been chosen to create data-sets for the density, the Young's modulus and the Poisson's ratio. Three isokom temperatures of the dynamic viscosity have been also investigated to determine the dynamic viscosity. A choice of oxides has been done sharing between five network formers, ten network modifiers and five network intermediates. Data-sets have been determined to be the largest possible.

The mechanical properties have been fitted based on theoretical models taken from literature. Instead of to fit the glass density, an artificial neural network is determined on the molar volume. By this way, the dependence on the molar mass is mathematically taken into account. The Young's modulus is also determined using the Makishima-Mckenzie model to account for the dissociation energy. The fitting is then done on the atomic packing fraction which is a dimensionless factor of the order of magnitude of

one. This quantity is crucial in the elasticity property since it is also involved in the Poisson's ratio. Using the model of Makishima and Mckenzie, the Poisson's ratio has been determined by fitting a parameter of the theoretical model. This inspired physical model improves significantly the prediction of the Poisson's ratio.

Finally, the melting, the softening and the annealing temperatures corresponding to a specific values of the dynamic viscosity have been fitting using artificial neural networks with three hidden layers and twenty neurons for each hidden layer. The determination of the dynamic viscosity is achieved using the well known VFT's law.

Property charts are also determined to see the influence of various glass families. By plotting the square root of a specific Young's modulus as a function of the melting temperature, phospho-silicate family gives the optimal specific modulus with the smallest melting temperature.

In this contribution, the relevance to take a physical-inspired model to fit a data-set of a mechanical property is clearly established. The work has to be extended to model the fracture toughness for which theoretical models exist. However, the number of data is limited even with the two databases used in this contribution. Moreover, the amount of data has to be increased for the Poisson's ratio as well.

This work is also the first step to explore new glass compositions which can be found by genetic algorithm for instance as already done in [46]. The development of Shapley additive explanation is also an analysis to explore to measure the importance of each oxide on a particular property. To enable to give properties with uncertainties, probabilistic neural networks could be also a perspective of this current work.

Credit author statement

F. Pigeonneau: Conceptualisation, Data curation, Investigation, Methodology, Software, Validation, Formal analysis, Writing - original draft. **M. Rondet**: Data curation, Investigation, Software, Methodology, Formal analysis, Writing - Review & Editing. **O. de Lataulade**: Conceptualisation, Supervision, Writing - Review & Editing. **E. Hachem**: Conceptualisation, Supervision, Project administration, Writing - Review & Editing.

Declaration of Competing Interest

The authors declare that they have no known competing financial interests or personal relationships that could have appeared to influence the work reported in this article.

References

[1] D. L. Morse and J. W. Evenson. Welcome to the glass age. *Int. J. Appl. Glass Sci.*, 7(4):409–412, 2016.

[2] J. C. Mauro and E. D. Zanotto. Two centuries of glass research: Historical trends, current status, and grand challenges for the future. *Int. J. Appl. Glass Sci.*, 5(3):313–327, 2014.

[3] H. Scholze. *Glass. Nature, Structures and Properties.* Springer-Verlag, Berlin, 1990.

[4] A. Winkelmann and O. Schott. Ueber die elasticität und über die zug- und druckfestigkeit verschiedener neuer gläser in ihrer abhängigkeit von der chemischen zusammensetzung. *Ann. Phys.*, 287(4):697–729, 1894.

[5] A. K. Varshneya and J. C. Mauro. *Fundamentals of Inorganic Glasses.* Elsevier, third edition, 2019.

[6] T. Lakatos, L. G. Johansson, and B. Simmingsköld. The effect of some glass components on the viscosity of glass. *Glasteknisk tidskrift*, 27(2):25–28, 1972.

[7] A. Fluegel. Glass viscosity calculation based on a global statistical modelling approach. *Glass Technol.: Eur. J. Glass Sci. Technol. A*, 48(1):13–30, 2007.

[8] A. Fluegel, D. A. Earl, A. K. Varshneya, and T. P. Seward. Density and thermal expansion calculation of silicate glass melts from 1000°C to 1400°C. *Phys. Chem. Glasses: Eur. J. Glass Sci. Technol. B*, 49(5):245–257, 2008.

[9] R. Ravinder, V. Venugopal, S. Bishnoi, S. Singh, M. Zaki, H. S. Grover, M. Bauchy, M. Agarwal, and N. M. A. Krishnan. Artificial intelligence and machine learning in glass science and technology: 21 challenges for the 21st century. *Int. J. Appl. Glass Sci.*, 12(3):277–292, 2021.

[10] M. Galushka, C. Swain, F. Browne, M. D. Mulvenna, R. Bond, and D. Gray. Prediction of chemical compounds properties using a deep learning model. *Neural Comput. Appl.*, 33(20):13345–13366, 2021.

[11] D. Jha, L. Ward, A. Paul, W.-K. Liao, A. Choudhary, C. Wolverton, and A. Agrawal. ElemNet: Deep learning the chemistry of materials from only elemental composition. *Sci. Rep.*, 8(1):17593, 2018.

[12] J. C. Mauro, A. Tandia, K. D. Vargheese, Y. Z. Mauro, and M. M. Smedskjaer. Accelerating the design of functional glasses through modeling. *Chem. Mater.*, 28(12):4267–4277, 2016.

[13] A. Tandia, M. C. Onbasli, and J. C. Mauro. Machine learning for glass modeling. In *Springer Handbook of Glass*, chapter 33, pages 1155–1190. Springer, 2019.

[14] S. Bishnoi, S. Singh, R. Ravinder, M. Bauchy, N. N. Gosvami, H. Kodamana, and N.M. A. Krishnan. Predicting Young's modulus of oxide glasses with sparse datasets using machine learning. *J. Non-Cryst. Solids*, 524:119643, 2019.

[15] B. Deng. Machine learning on density and elastic property of oxide glasses driven by large dataset. *J. Non-Cryst. Solids*, 529:119768, 2020.

[16] R. Ravinder, K. H. Sridhara, S. Bishnoi, H. S. Grover, M. Bauchy, Jayadeva, H. Kodamana, and N. M. A. Krishnan. Deep learning aided rational design of oxide glasses. *Mater. Horiz.*, 7:1819–1827, 2020.

[17] D. R. Cassar. ViscNet: Neural network for predicting the fragility index and the temperature-dependency of viscosity. *Acta Mater.*, 206:116602, 2021.

[18] M. Zaki, V. Venugopal, R. Bhattoo, S. Bishnoi, S. K. Singh, A. R. Allu, Jayadeva, and N. M. A. Krishnan. Interpreting the optical properties of oxide glasses with machine learning and shapely additive explanations. *J. Am. Ceram. Soc.*, 105(6):4046–4057, 2022.

[19] S. M. Lundberg and S.-I. Lee. A unified approach to interpreting model predictions. In *Advances in Neural Information Processing Systems*, 2017.

[20] C. Le Losq and B. Baldoni. Machine learning modeling of the atomic structure and physical properties of alkali and alkaline-earth aluminosilicate glasses and melts. *J. Non-Cryst. Solids*, 617:122481, 2023.

[21] S. Park, J. H. Fonseca, K. P. Marimuthu, C. Jeong, S. Lee, and H. Lee. Determination of material properties of bulk metallic glass using nanoindentation and artificial neural network. *Intermetallics*, 144:107492, 2022.

[22] K. Bobzin, H. Heinemann, E. Burbaum, L.M. Johann, J. Seßler, and J. Gärtner. Data driven development of iron-based metallic glasses using artificial neural networks. *J. Alloys Compd.*, 972:172895, 2024.

[23] A. Makishima and J. D. Mackenzie. Direct calculation of Young's modulus of glass. *J. Non-Cryst. Solids*, 12(1):35–45, 1973.

[24] A. Makishima and J. D. Mackenzie. Calculation of bulk modulus, shear modulus and poisson's ratio of glass. *J. Non-Cryst. Solids*, 17:147–157, 1975.

[25] S. Inaba, S. Fujino, and K. Morinaga. Young's modulus and compositional parameters of oxide glasses. *J. Am. Ceram. Soc.*, 82(12):3501–3507, 1999.

[26] J. Rocherullé, C. Ecolivet, M. Poulain, P. Verdier, and Y. Laurent. Elastic moduli of oxynitride glasses: Extension of Makishima and Mackenzie's theory. *J. Non-Cryst. Solids*, 108(2):187–193, 1989.

[27] Y. Shi, A. Tandia, B. Deng, S. R. Elliott, and M. Bauchy. Revisiting the Makishima-Mackenzie model for predicting the Young's modulus of oxide glasses. *Acta Mater.*, 195:252–262, 2020.

[28] M. Plucinski and J. W. Zwanziger. Topological constraints and the Makishima–Mackenzie model. *J. Non-Cryst. Solids*, 429:20–23, 2015.

[29] D. R. Cassar. GlassNet: A multitask deep neural network for predicting many glass properties. *Ceram. Int.*, 49(22):36013–36024, 2023.

[30] G. James, D. Witten, T. Hastie, R. Tibshirani, and J. Taylor. *An Introduction to Statistical Learning, With Applications in Python.* Springer, 2023.

[31] M. L. Huggins. The density of silicate glasses as a function of composition. *J. Opt. Soc. Am.*,

30(9):420–430, 1940.

[32] M. L. Huggins and K.-H. Sun. Calculation of density and optical constants of a glass from its composition in weight percentage. *J. Am. Ceram. Soc.*, 26(1):4–11, 1943.

[33] N. P. Bansal and R. H. Doremus. *Handbook of Glass Properties*. Academic Press, Inc., 1986.

[34] N. Soga. Elastic moduli and fracture toughness of glass. *J. Non-Cryst. Solids*, 73(1–3):305–313, 1985.

[35] T. Rouxel and S. Yoshida. The fracture toughness of inorganic glasses. *J. Am. Ceram. Soc.*, 100:4374–4396, 2017.

[36] M. H. Manghnani. Pressure and temperature studies of glass properties related to vibrational spectra. techreport NR 032-527, Hawaii Institute of Geophysic. University of Hawaii, 1974.

[37] M. Imaoka, H. Hasegawa, T. Hamaguchi, and Y. Kurotaki. Chemical composition and tensile strength of glasses in the B_2O_3-PbO and B_2O_3-SiO_2-Na_2O systems. *Yogyo Kyokai Shi*, 5:164–172, 1971.

[38] A. Farina, A. Klar, R. M. M. Mattheij, A. Mikelić, and N. Siedow. *Mathematical Models in the Manufacturing of Glass*. Springer, 2011.

[39] K.-U. Hess and D. B. Dingwell. Viscosities of hydrous leucogranitic melts: A non-Arrhenian model. *Am. Mineral.*, 81(9-10):1297–1300, 1996.

[40] J. C. Dyre. Colloquium: The glass transition and elastic models of glass-forming liquids. *Rev. Mod. Phys.*, 78(3):953–972, 2006.

[41] C. A. Angell. Spectroscopy simulation and scattering, and the medium range order problem in glass. *J. Non-Cryst. Solids*, 73(1–3):1–17, 1985.

[42] T. P. Seward III. Modeling of glass making processes for improved efficiency: High temperature glass melt property database for modelling. techreport DOE/EE41262-2, NYSCC, Alfred University, Alfred, NY (US), 2003.

[43] M. F. Ashby. *Materials selection in mechanical design*. Elsevier, 2011.

[44] N. Clark, S. Traugh, S. Astle, J. C. Mauro, M. F. L. Mancini, G. B. Cook, and C. E. Gallagher. Low-melting glass compositions, articles, and methods of making the same, 2023. Patent WO 2023/177659 A1.

[45] P. H. Morse and H. Feshbach. *Methods of theoretical physics*, volume Part I. McGraw-Hill book company, Inc., New York, 1953.

[46] D. R. Cassar, G. G. Santos, and E. D. Zanotto. Designing optical glasses by machine learning coupled with a genetic algorithm. *Ceram. Int.*, 47:10555–10564, 2021.